Taylor & Francis
Taylor & Francis Group

ORIGINAL ARTICLE

⊞ OPEN ACCESS   Check for updates

Concrete damage analysis based on higher-order beam theories using fracture energy regularization

J. Shen[a], M. R. T Arruda[b], and A. Pagani[a]   iD

[a]Mul2 Group, Department of Mechanical and Aerospace Engineering, Politecnico di Torino, Torino, Italy; [b]CERIS, Instituto Superior Técnico, Universidade de Lisboa, Lisbon, Portugal

ABSTRACT

This paper presents the numerical damage analysis of concrete structures using higher-order beam theories based on Carrera Unified Formulation (CUF). The concrete constitutive relation is modeled using continuum damage mechanics based on a modified Mazars concrete damage model, in which both the tensile and compressive softening behaviors are regularized with classical fracture energy methodology. An expression is proposed to estimate the characteristic length in higher-order beam theories, to prevent mesh dependency. Both softening constitutive laws and fracture energy calculations are obtained according to Model Code 2010. To assess the efficiency of the proposed model, three classical benchmark quasi-static experiments are taken for validation. From the comparison between numerical and experimental results, the proposed CUF model using continuum damage mechanics can present 3D accuracy with low computational costs and reduce the mesh dependency.

1. Introduction

In quasi brittle materials, such as concrete, the crack propagation is a nonlinear problem because the fracture process zone (FPZ) is non-negligible and mainly an irreversible process. The difficulty of concrete finite element (FE) modeling is that the tensile strain presents a softening constitutive response at the FPZ due to the generation and propagation of microcracks, which could lead to localization instability.

1.1. Literature review

Over the past years, several researchers proposed different theories to simulate concrete behavior successfully in the framework of continuum media, such as plasticity [1] and continuum damage mechanics (CDM). In the framework of CDM, the most popular models are: isotropic damage models [2, 3], anisotropic damage models [4, 5], and plastic-damage models [6–8].

Though the above approaches can work in some specific cases, localization instability with consequent zero energy dissipation and sensitivity to mesh size are severe difficulties in finite element simulations of quasi-brittle failure [9]. To overcome those challenges, a well-known approach is the nonlocal models, including integral [10, 11] and gradient models [12], where a material point is associated with the stress both from local point and neighbor points. This

model can prevent spurious localization from converging to failure at zero energy dissipation. However, the treatments of weighting function near the structural boundary are difficult. Some improvements are taken, such as the nonlocal boundary layer model [13], to eliminate the boundary problem, but they are not based on physical arguments [14].

Inspired by the cohesive crack model or fictitious crack model that was proposed by Hillerborg [15], Bažant and Oh developed another approach called crack band model (CBM) [16]. In this approach, a tensorial damage constitutive law is applied to consider the effect of the normal stresses parallel to the crack plane [13]. To preserve the fracture energy and mitigate the spurious mesh dependence, a material characteristic size h_e is introduced to adjust the material's constitutive relations of each Gauss point. The value of h_e normally sets to be equal to the crack bandwidth. In [13], h_e is defined as the minimum possible spacing of parallel cracks when the cracks do not localize. Later, Le [17] and Gorgogianni [18] extended the CBM to stochastic FE simulations and rate-dependent constitutive behavior when meeting the mesh size or material length is larger than the crack bandwidth.

Among the previous damage models, the isotropic damage model with a tension and compression damage variable developed by Mazars [3] is quite useful because it can describe the strain-softening of the concrete only by using two scalar damage variables, while others need numerous

---

CONTACT A. Pagani ✉ alfonso.pagani@polito.it   Mul2 Group, Department of Mechanical and Aerospace Engineering, Politecnico di Torino, Corso Duca degli Abruzzi 24, 10129 Torino, Italy.

parameters whose physical meaning may be unclear. Mazars damage model [3] is convenient for non-linear structural design, due to its simple formulation and few input values.

So far, the Mazars damage model has been coupled with various regularization techniques such as non-local regularization [19] and tensile fracture energy regularization [20]. However, the previously adopted stress-strain constitutive relations in [20] are not representative of engineering design. Besides, the method from [20] is not truly mesh independent by limiting the maximum mesh size. Recently, Arruda [21] made a great improvement by implementing the stress-strain constitutive laws from practical concrete design code, such as fib Model Code 2010 (MC2010) [22]. Furthermore, Arruda [21] used a fracture energy regularization, for tensile and compressive behavior, by considering the post-peak slope of the constitutive curve as a function of the element size. Though it worked well in [21], only two-dimensional (2D) analysis with reduced integration was conducted via ABAQUS user subroutines, which means full three-dimensional (3D) analysis will take heavy computational costs.

When it comes to the efficiency of finite element calculation, the Carrera unified formulation (CUF) [23] is a powerful tool that considers the order of the model as an input of the analysis. Classical beam theories, Euler–Bernoulli beam model (EBBM) [24] and Timoshenko beam model (TBM) [25], can be obtained as particular cases. In CUF, higher-order one-dimensional (1D) models are adopted and the 3D displacement field can be evaluated compactly as an arbitrary order expansion in terms of generic functions. The comprehensive discussion about CUF can be found in [26]. More recently, Lagrange polynomials have been used to discretize the cross-sectional kinematics [27, 28]. So far, CUF has been employed to the progressive damage analysis of composite structures with the crack band theory [29–31]. Regarding to civil structures, CUF was also employed for the investigation of reinforced concrete structures [32, 33] and steel-concrete composite structures [34], but with limitations either on the use of linear analysis or on limited sections with a equivalent single layer.

1.2. Research significance

Motivated by the foregoing discussion, the authors try to expand the CUF to the nonlinear fracture analysis of concrete structures because CUF is a powerful formulation that can produce accurate results with lower computational costs. To avoid mesh sensitivity and other ill-posed problems, a general and robust fracture energy regularization in CUF is developed and proposed. For this concrete damage model, fib Model Code 2010 [22] provides the practical tensile and compressive stress-strain constitutive relations of concrete. The post-peak region of the stress-strain relation for each Gauss point is relevant with the characteristic element length L_c, which ensures the larger elements will own smaller volumetric fracture energy and the smaller elements will have larger volumetric fracture energy. A new formula for calculating L_c, which is different from those in [29, 30], is proposed to do fracture energy regularization with higher-order

theories in CUF. This work will fill the gap in knowledge about nonlinear concrete fracture analysis via CUF.

1.3. Organization

This paper is organized as follows: First, the Lagrange expansion (LE) CUF model is presented. Then, the original damage model and modified damage model are introduced receptively. Meanwhile, the discussion on L_c in CUF is presented. Next, the model validation and associated concrete damage examples are shown to prove the accuracy of the proposed model, and directly compared with experimental values. Finally, some meaningful conclusions based on the above analysis are obtained.

2. Higher-order beam models

The finite elements that are formulated based on CUF are introduced first. A one-dimensional beam model is applied and some polynomial expansions are adopted to express cross-sectional kinematics approximation. Therefore, the full 3D results can be attained with quite low computational costs. The basic ideas and the main advantages of CUF are shown in this section.

2.1. Carrera unified formulation

Assuming a structure is aligned along the y axis, and the cross-section Ω is normal to the axis y. Then, in the framework of the CUF, the 3D displacement field of a beam model can be expressed as follows:

$$\mathbf{u}(x,y,z) = F_\tau(x,z)\mathbf{u}_\tau(y), \qquad \tau = 1,2,....,M \qquad (1)$$

where F_τ varies within the cross-section; $\mathbf{u}_\tau$ is the generalized displacements vector and M stands for the number of terms in the expansion. According to the Einstein notation, the repeated subscript τ indicates summation. The choice of F_τ and M is arbitrary, that is, different base functions of any order can be taken into account to model the kinematic field of a beam above the cross-section [26].

In this work, Lagrange-like polynomials are adopted as cross-section expanding functions F_τ, which is called the Lagrange expansion (LE). They are useful to deal with the arbitrary-shaped cross-section. Several Lagrange polynomials can be employed to develop higher-order beam theories, such as three-point linear (L3), four-point bilinear (L4), nine-point quadratic (L9), sixteen-point cubic (L16), etc. All Lagrange polynomials and their corresponding functions can be found in [26]. Here, the interpolation functions for the nine-point (L9) quadratic polynomial element are shown as an example:

$$F_\tau = \frac{1}{4}(r^2 + r\,r_\tau)(s^2 + s\,s_\tau), \quad \tau = 1,3,5,7$$
$$F_\tau = \frac{1}{2}s_\tau^2(s^2 + s\,s_\tau)(1 - r^2) + \frac{1}{2}r_\tau^2(r^2 + r\,r_\tau)(1 - s^2), \quad \tau = 2,4,6,8$$
$$F_\tau = (1 - r^2)(1 - s^2), \quad \tau = 9$$

$$(2)$$

where r and s are the normalized coordinates that vary from -1 to 1 and r_τ and s_τ are the actual coordinates of the nine nodes.

Then, the complete displacement field Eq. (1) can be given by one single L9 element as follows:

$$u_x(x, y, z) = F_1(x, z)u_{x1}(y) + F_2(x, z)u_{x2}(y) + \cdots + F_9(x, z)u_{x9}(y)$$
$$u_y(x, y, z) = F_1(x, z)u_{y1}(y) + F_2(x, z)u_{y2}(y) + \cdots + F_9(x, z)u_{y9}(y)$$
$$u_z(x, y, z) = F_1(x, z)u_{z1}(y) + F_2(x, z)u_{z2}(y) + \cdots + F_9(x, z)u_{z9}(y)$$
$$(3)$$

where $u_{x1}(y), ..., u_{z9}(y)$ are the unknown variables of the problem and represent the translational displacement components of nine points for each L9 element.

2.2. Finite element approach

The finite element approach can be adopted here to approximate the generalized displacements $\mathbf{u}_\tau$ by using the classical beam shape functions. Then, the displacement field Eq. (1) can be expressed as:

$$\mathbf{u}(x, y, z) = F_\tau(x, z)N_i(y)\mathbf{u}_{\tau i}, \qquad i = 1, ..., N_{NE} \quad (4)$$

where N_i stands for the shape functions of beam elements, N_{NE} is the number of nodes per beam element, and $\mathbf{u}_{\tau i}$ is the nodal displacement vector.

Normally, beam elements with two nodes (B2), three nodes (B3), and four nodes (B4) are available for choice according to the structural problem. In other words, the beam finite elements' choice is entirely independent of the cross-section discretization.

The governing equation of static problems can be derived by the Principle of Virtual Displacements (PVD), which is shown as follows:

$$\delta L_{int} = \delta L_{ext} \quad (5)$$

where L_{int} is the internal elastic work, L_{ext} is the work done by the external forces, and δ indicates the virtual variation. The virtual variation of the internal work is

$$\delta L_{int} = \int_V \delta \boldsymbol{\varepsilon}^T \boldsymbol{\sigma} \, dV \quad (6)$$

where $\boldsymbol{\varepsilon}$ is the strain vector, $\boldsymbol{\sigma}$ is the stress vector. Substituting the constitutive relations and Eq. (4) into Eq. (6) and the internal work can be rewritten in the following compact form:

$$\delta L_{int} = \delta \boldsymbol{u}_{sj}^T \mathbf{K}^{\tau sij} \mathbf{u}_{\tau i} \quad (7)$$

where $\mathbf{K}^{\tau sij}$ is the element stiffness matrix in the form of the 3×3 fundamental nucleus. Each element stiffness matrix can be formulated automatically according to four indexes τ, s, i, and j. The detailed derivation and the explicit expression of stiffness matrix can be found in [26].

The virtual work done by the external loads is

$$\delta L_{ext} = \int_V \delta \mathbf{u}^T \mathbf{g} \, dV + \int_S \delta \mathbf{u}^T \mathbf{p} \, dS + \int_L \delta \mathbf{u}^T \mathbf{q} \, dy + \delta \mathbf{u}^T \mathbf{P} \quad (8)$$

where $\mathbf{g}$ are the volume forces, $\mathbf{p}$ are the surface forces, $\mathbf{q}$ are the line forces and $\mathbf{P}$ are the concentrated loads. For the sake of simplicity, the external work can be rewritten in a weak form:

$$\delta L_{ext} = \delta \mathbf{u}_{sj}^T \mathbf{F} \quad (9)$$

where $\mathbf{F}$ is the nodal external force vector contributed by all external forces.

Finally, substituting Eqs. (7) and (9) into Eq. (5), the governing equation can be attained as:

$$\mathbf{K}^{\tau sij} \mathbf{u}_{\tau i} = \mathbf{F} \quad (10)$$

3. Mazars damage model

The elastic damage isotropic model for concrete proposed by Mazars [3] has the following characteristics: (1) Concrete behavior is a combination of elasticity and damage without permanent strains; (2) One scalar damage variable is assumed to be isotropic and directly influences the stiffness of the material; (3) The positive strain-based damage criteria are adopted. In real structures, the plastic strains from steel bars play a more important role than that from concrete when studying the cyclic or dynamic behaviors. Therefore, the Mazars damage model can work well when the concrete structures are under monotonic static load, though no permanent strains are taken into account.

3.1. Model formulation

The concrete damage constitutive law of Mazars [3] was defined as:

$$\boldsymbol{\sigma} = (1 - d)\mathbf{E_0}\boldsymbol{\varepsilon} \quad (11)$$

where matrix $\mathbf{E_0}$ is the local stiffness matrix for the undamaged concrete material and d is the variable of damage that is used to monitor the degradation of the material elasticity.

Mazars [3] expressed that the accumulated positive tensile principal strains accounted for damage evolution. Therefore, the damage evolution conditions are determined by the following loading function:

$$f = \varepsilon_{eq} - \varepsilon_{d0}(d) \quad (12)$$

where ε_{eq} represents the equivalent strain which can be calculated according to Eq. (13) using the positive principle effective strain vector because only positive strains produce damage in the Mazars model. The variable $\varepsilon_{d0}(d)$ is the hardening-softening parameter that determines the onset of elastic degradation of concrete material. The value of $\varepsilon_{d0}(d)$ is constant according to the ultimate tensile strain of material and will be updated as the equivalent strain after the damage occurs.

$$\varepsilon_{eq} = \sqrt{\langle \varepsilon_1 \rangle_+^2 + \langle \varepsilon_2 \rangle_+^2 + \langle \varepsilon_3 \rangle_+^2} \quad (13)$$

with

$$\langle a \rangle_\pm = \frac{1}{2}(a \pm |a|) \quad (14)$$

3.2. Original damage evolution

Damage onset is governed by the loading function. If $f < 0$ in Eq. (12), the structure works in elastic behavior and no

damage is detected. Once $f \geq 0$ in Eq. (12), the damage is activated and the value of d is defined as Eq. (15), which represents a linear combination of two scalar variables d_t and d_c.

$$d = \alpha_t^\beta d_t + \alpha_c^\beta d_c \qquad (15)$$

where β is a coefficient introduced to consider shear behavior, which can be set as 1.0 from [19] to underestimate the shear strength of the material. The variables d_t and d_c represent the damages caused by tensile and compressive behavior, respectively. To avoid any iterative process, Mazars [3] suggested both variables from Eq. (15) can be calculated directly using the following equations:

$$\begin{aligned} d_t &= 1 - \frac{(1 - A_t)\varepsilon_{d0}}{\varepsilon_{eq}} - A_t \exp\left(-B_t(\varepsilon_{eq} - \varepsilon_{d0})\right) \\ d_c &= 1 - \frac{(1 - A_c)\varepsilon_{d0}}{\varepsilon_{eq}} - A_c \exp\left(-B_c(\varepsilon_{eq} - \varepsilon_{d0})\right) \end{aligned} \qquad (16)$$

where A_t, A_c, B_t and B_c are the concrete material coefficients that can be obtained by fitting to data from classical uniaxial experiments [35].

The variables α_t and α_c from Eq. (15) are two parameters that can account for the influence of tensile and compressive behavior on total damage, respectively. Before obtaining their values, it is necessary to adjust the tensile strain vector ε_t and compressive strain vector ε_c using the principle positive effective stresses as follows:

$$\begin{aligned} \varepsilon_{t_i} &= \frac{1 + \nu}{E}\langle\hat{\sigma}_i\rangle_+ - \frac{\nu}{E}\sum_k \langle\hat{\sigma}_k\rangle_+ \\ \varepsilon_{c_i} &= \frac{1 + \nu}{E}\langle\hat{\sigma}_i\rangle_- - \frac{\nu}{E}\sum_k \langle\hat{\sigma}_k\rangle_- \end{aligned} \qquad (17)$$

where ν and E represent Poisson's ratio and elastic modulus of concrete materials, respectively.

Then, the total adjusted positive strain ε_V^+ can be calculated by summing up all positive elements from vector ε_t and ε_c. Furthermore, the variables α_t and α_c are obtained using Eq. (18).

$$\begin{aligned} \varepsilon_V^+ &= \sum_i \langle\varepsilon_{ti}\rangle_+ + \sum_i \langle\varepsilon_{ci}\rangle_+ \\ \alpha_t &= \frac{\sum_i \langle\varepsilon_{ti}\rangle_+}{\varepsilon_V^+}; \alpha_c = \frac{\sum_i \langle\varepsilon_{ci}\rangle_+}{\varepsilon_V^+} \end{aligned} \qquad (18)$$

3.3. Modification via regularization of fracture energy

The fracture energy regularization is an essential concept in the conventional CBM [16], which can be adopted here for the Mazars damage model to update the damage evolution laws for tensile and compressive behavior and further to avoid unrealistic collapses in FE simulations.

The stress-strain constitutive relation of concrete can be characterized by the elastic modulus E, the tensile strength f_{ctm} or compressive strength f_{cm}, and the fracture energy containing the tensile one G_{ft} and the compressive one G_{fc}. The softening branch of stress-strain curve is determined by fracture energy. Once the mesh size get changed in FE

simulation, the post-peak part of the stress-strain curve also needs adjustment to preserve the fracture energy.

In fracture energy regularization, the material element size h_e is introduced to get the total energy dissipation density containing the tensile one g_{ft} and the compressive one g_{fc}. The total energy dissipation density, also named the volumetric fracture energy in [21], is defined as the area under the uniaxial stress-strain curve. Then, the softening branch of stress-strain relation for each Gauss point in FE simulation will depend on the volumetric fracture energy rather than fracture energy. The tensile softening branch of stress-strain curve can be rescaled by the material element size h_e, which is expressed as:

$$g_{ft} = \frac{G_{ft}}{h_e} \qquad (19)$$

and the corresponding compressive softening relation for each Gauss point can be rescaled as:

$$g_{fc} = \frac{G_{fc}}{h_e} \qquad (20)$$

3.3.1. Characteristic element lengths

Evidently, the material element size h_e is determined by the FE mesh size. For CDM models in a FE framework, a scalar characteristic element length L_c is provided to the material model [36], which means the h_e in Eqs. (19) and (20) can be replaced with L_c.

The definition of L_c is the cube root of the element volume V for a 3D element or the square root of the element area A for a 2D element in commercial software tools such as ABAQUS [37], which can be expressed as:

$$L_{c,V} = \sqrt[3]{V} \qquad \text{or} \qquad L_{c,A} = \sqrt{A} \qquad (21)$$

According to [38], the characteristic length (L_c) is affected by element type, shape, orientation, and the order of elements. It is referred that damage could localize into a single Gauss point for higher-order finite elements [38]. Thus, it is essential to take a proper adjustment for the L_c so that the global energy dissipation is captured correctly.

Other works [29, 30] on CUF for progressive damage of composite structures considered $L_c = (V_{GP})^{1/3}$, where V_{GP} is the Gauss point volume of the given element. The Gauss point volume is the share of the element volume at each Gauss point.

Given the aforementioned consideration, one beam element and one Lagrange element in CUF can be considered to form a 3D element with a volume. Then the volume should be divided by one parameter to consider the influence of element order. Therefore, the following equation is assumed to get L_c in CUF based FE simulations:

$$L_c = \sqrt[3]{\frac{A_e \times L_e}{(\sqrt{M} - 1)^2 \times (N_{NE} - 1)}} \qquad (22)$$

where A_e and L_e represent the area of one Lagrange element from cross-section and the length of one beam element, respectively.

For the fracture energy method to be properly applied, using the classical methodology, the elements must be near
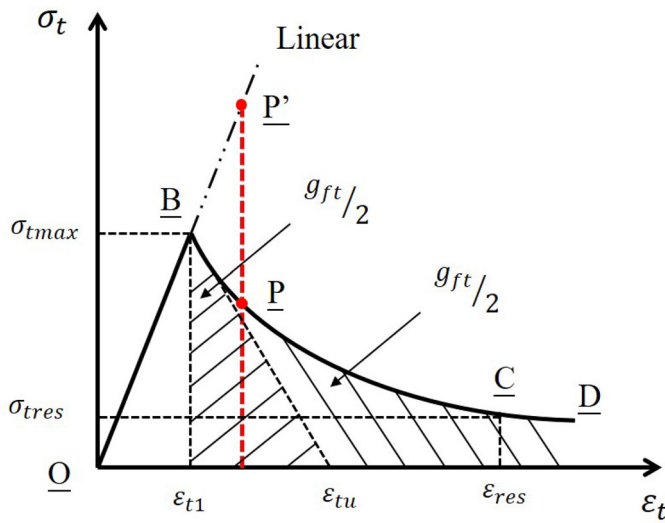
Figure 1. Stress-strain relation of concrete for uniaxial tension.

Figure 2. Stress-strain relation of concrete for uniaxial compression.

$$\sigma_{tmax} = f_{ctm}; \, \varepsilon_{t1} = \varepsilon_{d0}; \, \varepsilon_{tu} = \frac{G_{ft}}{L_c f_{ctm}} + \varepsilon_{t1}; \, p_t = \frac{\sigma_{tres}}{f_{ctm}}$$

where f_{ctm} is the mean uniaxial tensile strength of concrete; ε_{tu} is the equivalent ultimate strain for bilinear softening, which can be computed using the tangent to the exponential softening law at point B. σ_{tres} and ε_{tres} are the residual stresses and strains to make the value of damage not equal 1.0. The volumetric fracture energy g_{ft} is computed from the shaded parts of Figure 1.

3.3.3. Compression damage behavior

Figure 2 shows the stress-strain relation of concrete for uniaxial compression from MC2010 [22]. The initial relation (path OAB) from MC2010 [22] is used at first. The following is a simple bilinear softening branch (path $BCDE$) that is referred from [39]. To minimize the convergence problem, the model adopts a residual compressive strain (ε_{cres}) to let the value of stress never equal 0.0, which means the stress will be constant when the strain achieves ε_{cres}. The compression damage evolution law is defined by:

$$1 - d_c = \frac{\sigma_{cp}}{\sigma_{cp'}} \tag{26}$$

where σ_{cp} and $\sigma_{cp'}$ are the compressive stresses of any point P and P' corresponding to the constitutive model with damage and without damage, respectively.

Similarly, substituting the stress-strain relations into Eq. (26) and the detailed compression damage evolution law can be described as:

a square [21, 38]. For the case of higher-order beam theories, this is more complex, since the L_c from Eq. (22) may depend on four parameters. If not proper caution is taken, then an arbitrary use of these parameters can cause some convergence difficulty. Therefore, the following equation should be approximately satisfied in CUF for accuracy and convergence:

$$\frac{\sqrt{A_e}}{L_e} \approx \frac{\sqrt{M} - 1}{N_{NE} - 1} \tag{23}$$

3.3.2. Tensile damage behavior

The constitutive model of concrete tensile behavior is shown as Figure 1, which is proposed based on the stress-strain relation from MC2010 [22]. An initial nonlinear behavior that should occur in branch OA in MC2010 [22] is ignored due to the rapid cracking of the concrete at the initial stages of the structural response. A bilinear softening law in MC2010 [22] is replaced with a classical exponential softening law (branch BD) in Figure 1 to avoid convergence problems when the tensile stress approaches 0.0. The tension damage evolution law is defined by:

$$1 - d_t = \frac{\sigma_{tp}}{\sigma_{tp'}} \tag{24}$$

where σ_{tp} and $\sigma_{tp'}$ are the tensile stresses of any point P and P' corresponding to the constitutive model with damage and without damage, respectively.

Substituting the stress-strain relations into Eq. (24) and the detailed tension damage evolution law can be described as:

$$d_t = \begin{cases} 1 - \dfrac{\varepsilon_{d0}}{\varepsilon_{eq}} \exp\left(\dfrac{\varepsilon_{t1} - \varepsilon_{eq}}{\varepsilon_{tu} - \varepsilon_{t1}}\right) & \text{if} \quad \varepsilon_{eq} \leqslant \varepsilon_{tres} \\ 1 - \dfrac{p_t \times \varepsilon_{d0}}{\varepsilon_{eq}} & \text{if} \quad \varepsilon_{eq} > \varepsilon_{tres} \end{cases} \tag{25}$$

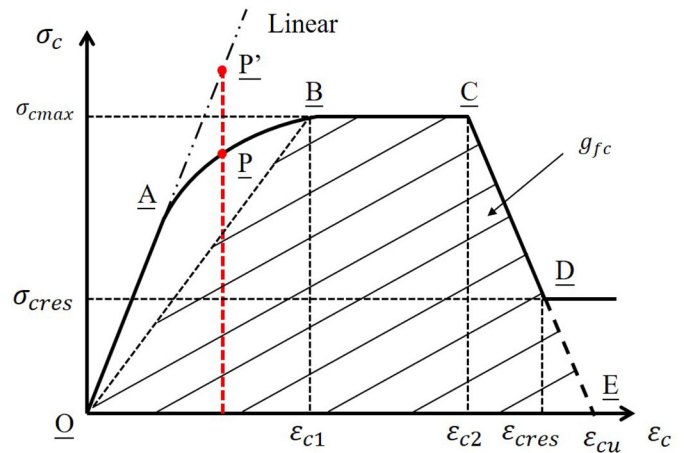All parameters and physical quantities present in Eq. (25) and Figure 1 are defined by:

$$d_c = \begin{cases} 1 - \dfrac{(k \times \bar{\varepsilon}_c - \bar{\varepsilon}_c^2) f_{cm}}{\left(1 + (k - 2) \times \bar{\varepsilon}_c\right) E_{cm} \varepsilon_{eqc}} & \text{if} \quad \varepsilon_{eqc} \leqslant \varepsilon_{c1} \\ 1 - \dfrac{f_{cm}}{E_{cm} \varepsilon_{eqc}} & \text{if} \quad \varepsilon_{c1} < \varepsilon_{eqc} \leqslant \varepsilon_{c2} \\ 1 + \dfrac{k_1}{E_{cm}} - \dfrac{k_2}{E_{cm} \varepsilon_{eqc}} & \text{if} \quad \varepsilon_{c2} < \varepsilon_{eqc} \leqslant \varepsilon_{cres} \\ 1 - \dfrac{p_c f_{cm}}{E_{cm} \varepsilon_{eqc}} & \text{if} \quad \varepsilon_{cres} < \varepsilon_{eqc} \end{cases}$$
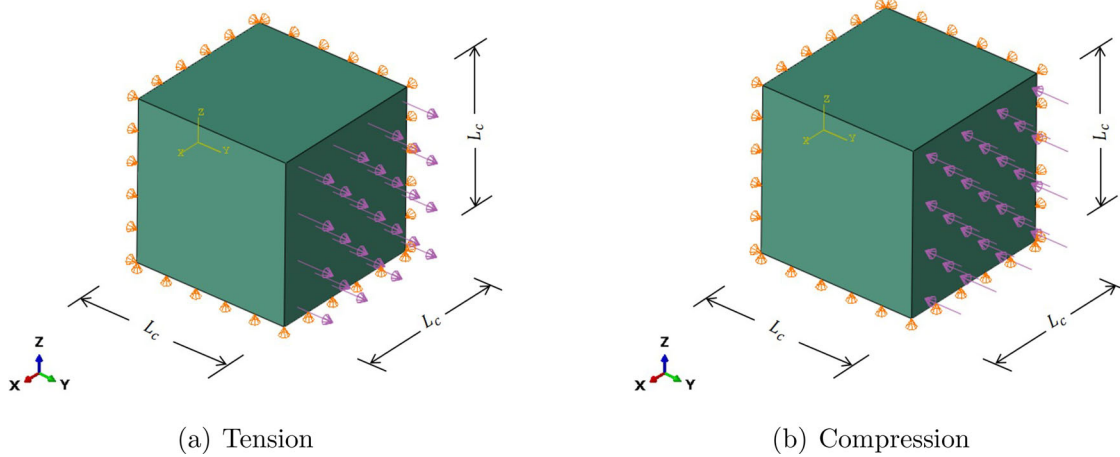
$$\tag{27}$$

(a) Tension

(b) Compression

Figure 3. Boundary conditions.

where

$$\sigma_{cmax} = f_{cm}; \quad \varepsilon_{eqc} = \frac{\varepsilon_{eq}}{\nu\sqrt{2}}; \quad \bar{\varepsilon}_c = \frac{\varepsilon_{eqc}}{\varepsilon_{c1}};$$

$$k = \frac{1.05 E_{cm}\varepsilon_{c1}}{f_{cm}}; \quad p_c = \frac{\sigma_{cres}}{f_{cm}} \tag{28}$$

$$k_1 = \frac{f_{cm}}{(\varepsilon_{cu} - \varepsilon_{c2})}; \quad k_2 = f_{cm} + k_1 \times \varepsilon_{c2}$$

In these equations, f_{cm} represents the mean compressive strength of the concrete; E_{cm} is the secant Young's modulus; ε_{eqc} is the equivalent compressive strain; ε_{c1} and ε_{c2} are the strain parameters taken as 2.0‰ and 2.4‰, respectively [40]; k are the parameters to describe the softening part in branch AB from EC2 [40]; k_1 and k_2 are the parameters to describe the softening curve in path CDE; $\bar{\varepsilon}_c$ is a unidimensional strain ratio provided in MC2010 [22]; ε_{cu} is the extreme strain that is computed by Eq. (29).

$$g_{fc} = \frac{G_{fc}}{L_c} = \sigma_{cmax} \times \left(\frac{\varepsilon_{cu} + (\varepsilon_{c2} - \varepsilon_{c1})}{2}\right) \tag{29}$$

When computing the volumetric fracture energy g_{fc}, the residual stress can be neglected from [41]. Therefore, g_{fc} can be computed from the shaded area in Figure 2.

4. Model validation

First, a representative single element analysis will be conducted to verify the implementation of modified Mazars model in CUF. A concrete cube is adopted to test the tensile and compressive behavior under the uniaxial tension and compression, respectively. The boundary conditions are shown in Figure 3.

The material properties are listed in Table 1, which belongs to the C30 strength class. The residual compressive stress and tensile stress are taken as the $0.5f_{cm}$ and $0.15f_{tm}$, respectively. The tensile fracture energy and compressive fracture energy can be computed by Eqs. (30) and (31) from MC2010 [22] and [42], respectively:

$$G_{ft} = 73 \times (f_{cm})^{0.18} \tag{30}$$

$$G_{fc} = 8.6 \times (f_{cm})^{0.25} \tag{31}$$

Table 1. Material properties.

| Material	E (GPa)	f_{ctm} (MPa)	f_{cm} (MPa)	v
Concrete	30	2.9	38	0.2

In this case, three different sizes of the cube are calculated whose side lengths are 1 m, 0.5 m, and 0.1 m, respectively. Only one L4 element and one B2 element are adopted so that the L_c will be equal to the cube side length.

The calculated strain-stress curves are shown in Figure 4. The curves are similar to the constitutive relations both from the tensile behavior from Figure 1 and compressive behavior from Figure 2. For one thing, the maximum compressive and tensile stress are the same regardless of the value of L_c. For the other, the softening parts are influenced by the value of L_c. The smaller the L_c is, the larger the volumetric fracture energy is, which further leads to the model being less brittle. In other words, the fracture energy is preserved successfully by using Eqs. (19) and (20).

Furthermore, a cube with a side length of 1 m is taken for further study. More configurations can be adopted here to study the influence of the order of elements. The L_c can be computed from Eq. (22). For example, one B3 element and one L9 element are both quadratic, and then the corresponding L_c should be 0.5 m. One B4 element and one L16 element are both cubic, and then the corresponding L_c is around 0.33 m.

From the tensile curves in Figure 5(a), the model with different orders shows the same results before the peak and shows the different softening curves because different L_c is produced. For compressive behavior in Figure 5(b), the curve from a full linear model (L4 + B2) is similar to that from a full quadratic model (L9 + B3). Then the full cubic model (L16 + B4) shows a different post-peak slope because the corresponding L_c gets a sharp decrease.

Overall, the tensile and compressive stress-strain curves are plotted as expected from [22]. The constitutive laws are mainly influenced by the volumetric fracture energy that is determined by Eqs. (19) and (20). Therefore, the fracture energy regularization technique is applied successfully and the value of L_c in CUF can be correctly calculated by Eq. (22).
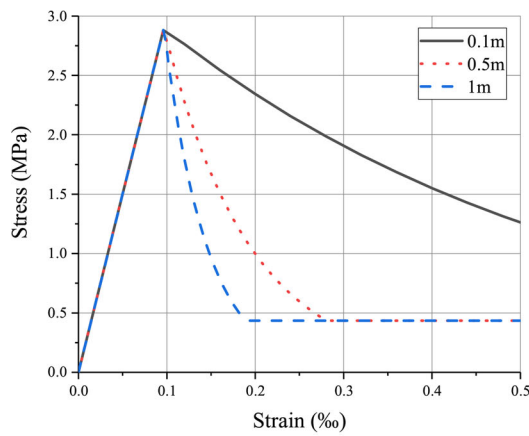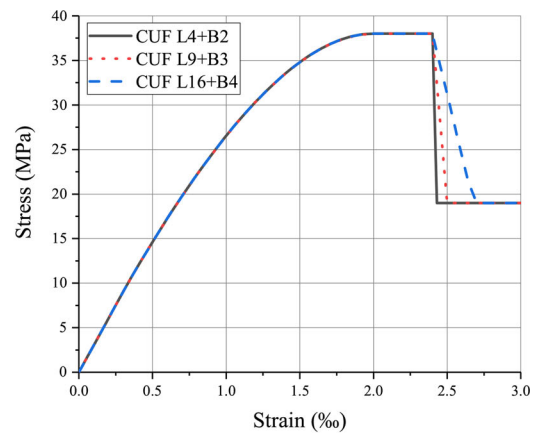
(a) Tension
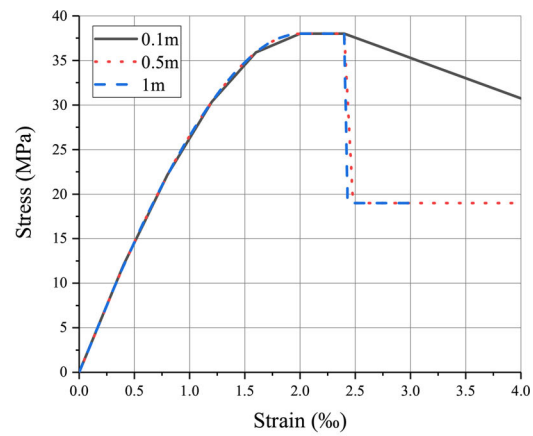
(b) Compression

Figure 4. The effect of L_c on stress-strain curves.
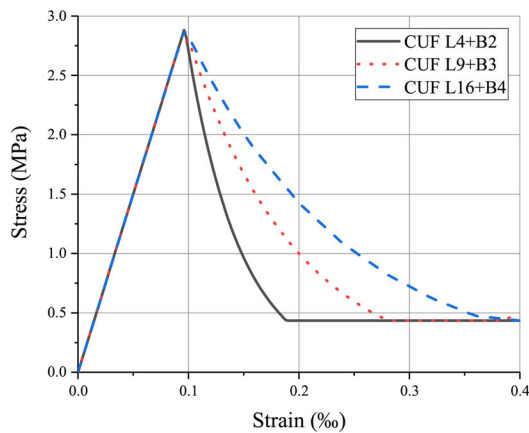
(a) Tension

(b) Compression

Figure 5. The effect of CUF expansion order on stress-strain curves.

5. Numerical results

In this section, three known benchmarks in the scientific community are tested using the CUF formulation with CDM. The displacement-control method is adopted to solve the quasi-static nonlinear structural problems. To highlight the capability of the CUF, the numerical study is performed using the beam axis perpendicular or parallel to the analyzed structure, something not possible with classical beam theories.

5.1. The L-shaped panel test

An experimental benchmark for the validation of plain concrete cracking is provided in [43]. The geometric information and boundary conditions for numerical simulation are shown in Figure 6. The detailed material properties are listed in Table 2. The fracture energy is given by $G_f = 90 N/m$. Two upward vertical displacements are imposed as shown in Figure 6. To prevent any localized effects resulting from the

prescribed displacement, steel material is adopted for the right part boundary.

CUF models consist of Lagrange elements on cross-section and beam elements along the y-axis, respectively, which can be seen in Figure 7. The y-axis is along with the thickness and the cross-section is on the rest x-z plane. The order of LEs and beam elements are independent of each other, which can be considered as inputs according to needs. The higher-order elements are first considered here because L9 and L16 are more recommended than L4 in other applications of CUF [34]. Four kinds of model configurations are listed in Table 3. The second-order elements, L9 and B3, are adopted here. The number of Lagrange elements and beam elements are determined by satisfying Eq. (23) as far as possible.

From Figure 8, the final damage distributions of the L-shape panel are stable though different meshes are adopted, illustrating the mesh independence clearly. The damage propagation of the Model 3 is plotted in Figure 9. The
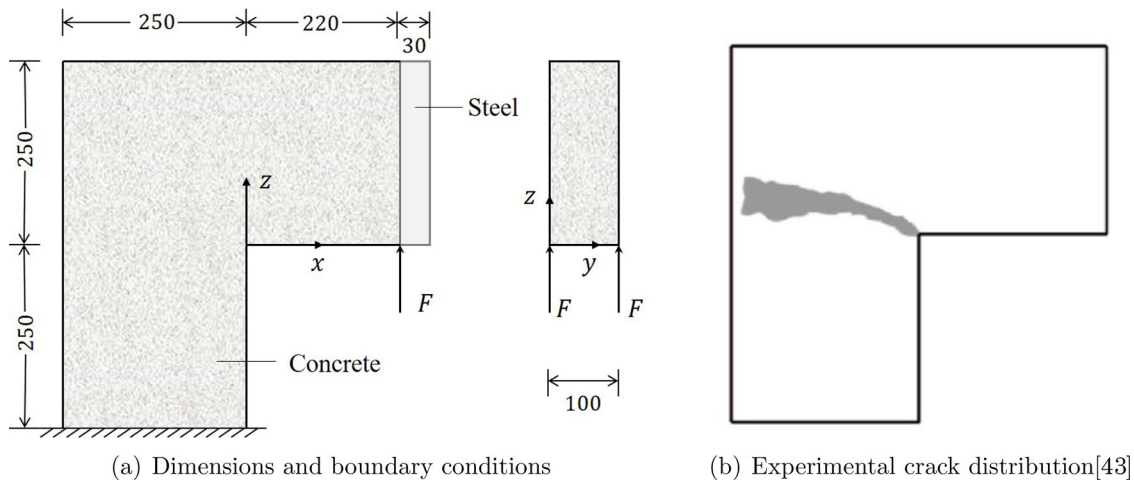
(a) Dimensions and boundary conditions

(b) Experimental crack distribution[43]

Figure 6. Dimensions and real crack distribution of the L-shaped panel (Unit: mm).

Table 2. Material properties of concrete in L-shaped panel test.

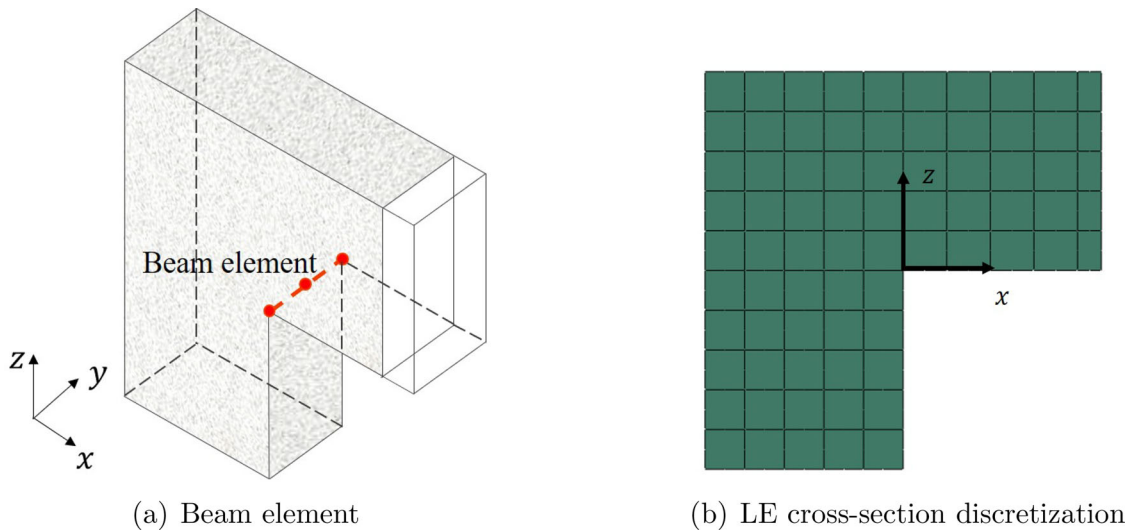| Material	E (GPa)	f_{ctm} (MPa)	f_{cm} (MPa)	υ
Concrete	26	2.5	31	0.18

(a) Beam element

(b) LE cross-section discretization

Figure 7. Mesh assignment of L-shape panel.

Table 3. Mesh configuration for L-shape panel.

Model No.	Model 1	Model 2	Model 3	Model 4
Configurations	75L9 + 2B3	192L9 + 3B3	300L9 + 4B3	507L9 + 5B3
LE side length (mm)	50	30	25	20
Beam element length (mm)	50	33.3	25	20
Characteristic length (mm)	25	16	12.5	9.8
DOFs	5115	17,493	34,587	57,591

damage first occurs at the reentrant corner. Then it evolves diagonally upwards, which is consistent with experimental crack distribution from Figure 6. After that, it propagates horizontally, which shows difference from experimental crack distribution. However, the whole propagation is more reasonable than that shown from [21] where traditional FE method was used.

Figure 10 shows the load-displacement curves of the L-shaped panel both from CUF models and experiments. From the stiffness, the peak load, and the softening part of curves in Figure 10, it is obvious that all numerical results are quite close to the experimental results, which also demonstrates the results are independent of the mesh size. It is worth noting that the stiffness and peak loads from different CUF models are slightly greater than the experimental ones. This phenomenon is also pointed out by [21], which is reasonable. For one thing, there was some uncertainty about the boundary conditions of the experiments. For the other, an assumption that
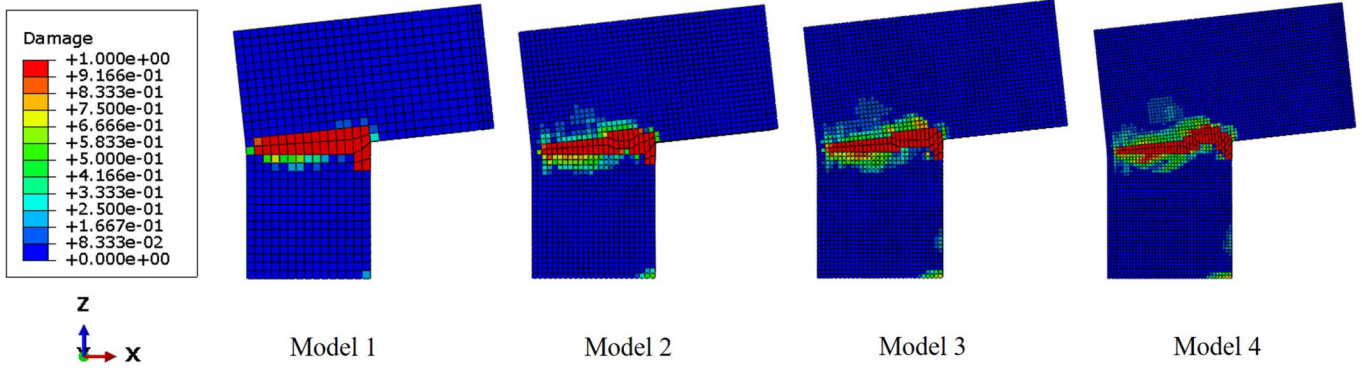
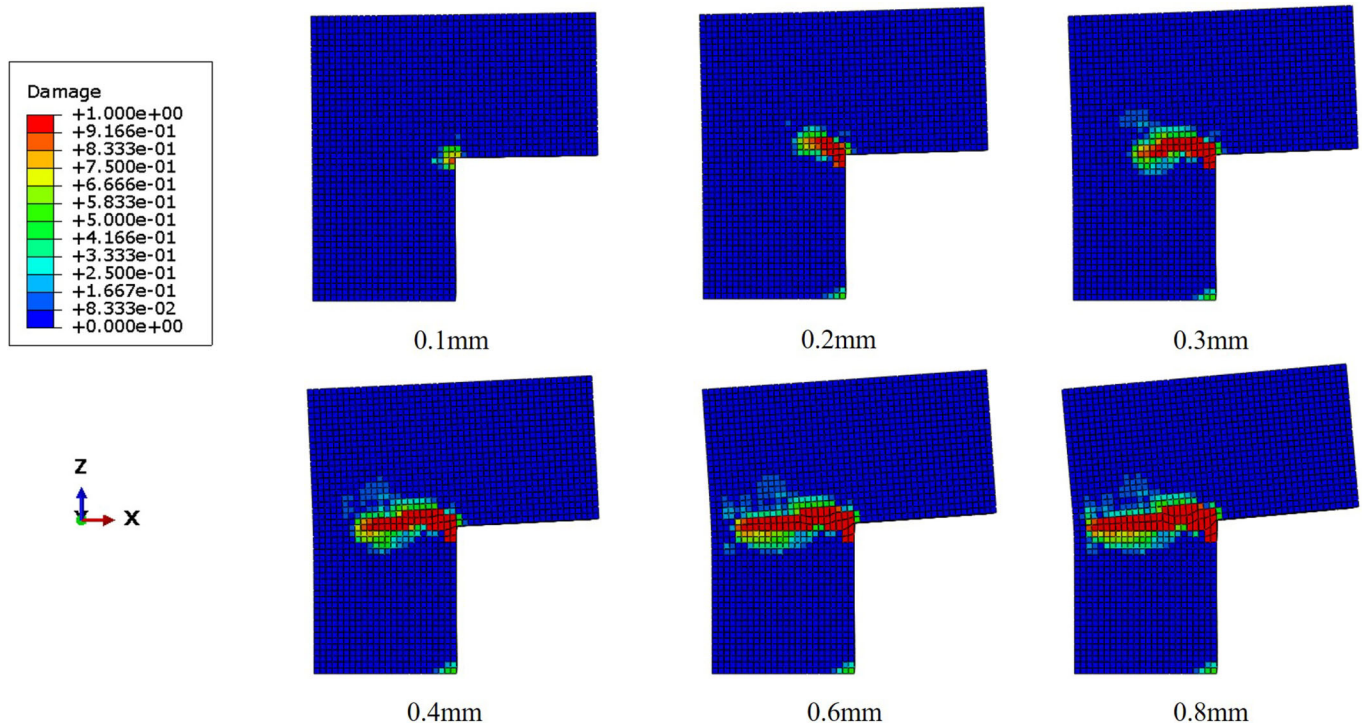**Figure 8.** Final damage distribution of panels for each model.

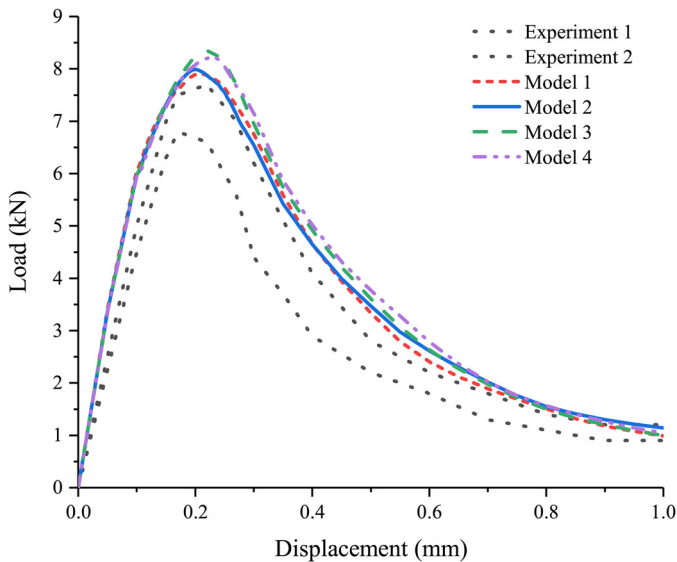**Figure 9.** Damage propagation of panel for Model 3.

Figure 10. Load-displacement curves of the L-shaped panel test.

the steel-like material is adopted close to the loading point during simulations provides extra stiffness and load-bearing capacity. Besides, the peak loads from Model 3 and Model 4 are marginally larger than those from Model 1 and Model 2. This can be attributed to Eq. (23) not being fully satisfied. In any case, Model 1 with the most coarse meshes and lowest DOFs is still able to accurately predict the structural response in terms of force versus displacement curve.

5.2. The Hassanzadeh test

Another well-known experimental concrete damage test called "Hassanzadeh test" was first conducted in [44]. Figure 11 shows the geometry of the plain concrete specimen with four edges notched in the middle. The bottom surface is fixed and the tension is imposed on the top via displacement control. Unlike the past similar simulations [21] where a 2D analysis is conducted, the full 3D simulation based on CUF will be
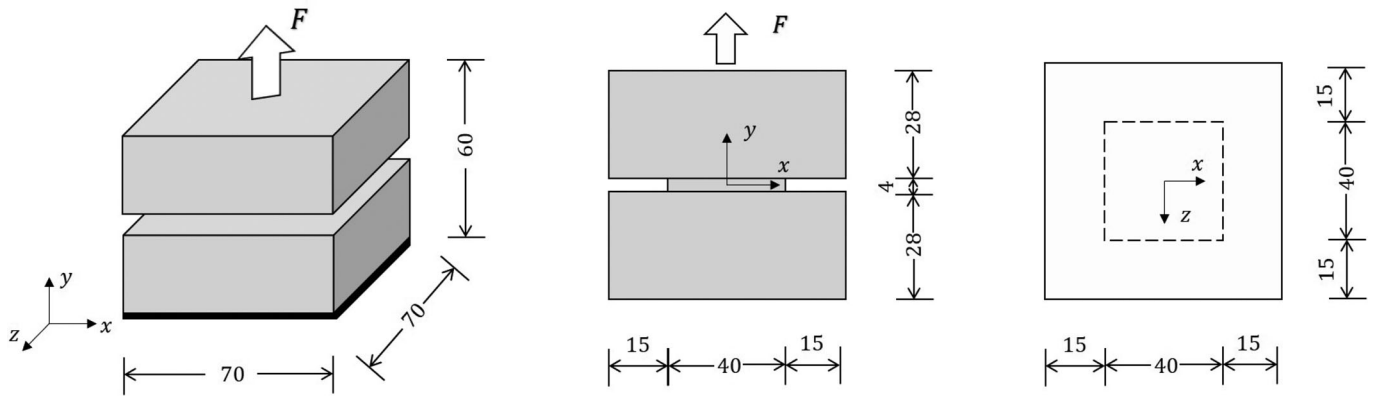
Figure 11. Dimensions of specimen in Hassanzadeh test (Unit: mm).

Table 4. Material properties of concrete in Hassanzadeh test.

Material	E (GPa)	f_{ctm} (MPa)	f_{cm} (MPa)	υ
Concrete	36	3.5	40	0.2

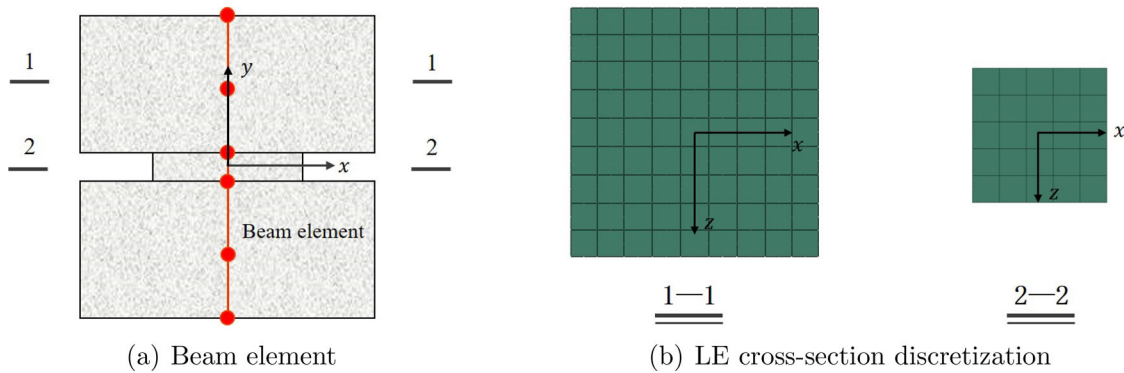
(a) Beam element (b) LE cross-section discretization

Figure 12. Mesh assignment of the specimen in Hassanzadeh test.

Table 5. Mesh configuration of the middle notched part in Hassanzadeh test.

Model No.	Model A	Model B	Model C	Model D
Middle configuration	25L9 + 1B2	64L9 + 1B4	64L16 + 1B4	100L16 + 1B4
LE side length (mm)	8.00	5.00	5.00	4.00
Beam element length (mm)	4.00	4.00	4.00	4.00
Characteristic length (mm)	4.00	2.03	1.55	1.33
Total DOFs	6498	16,734	36,606	50,142
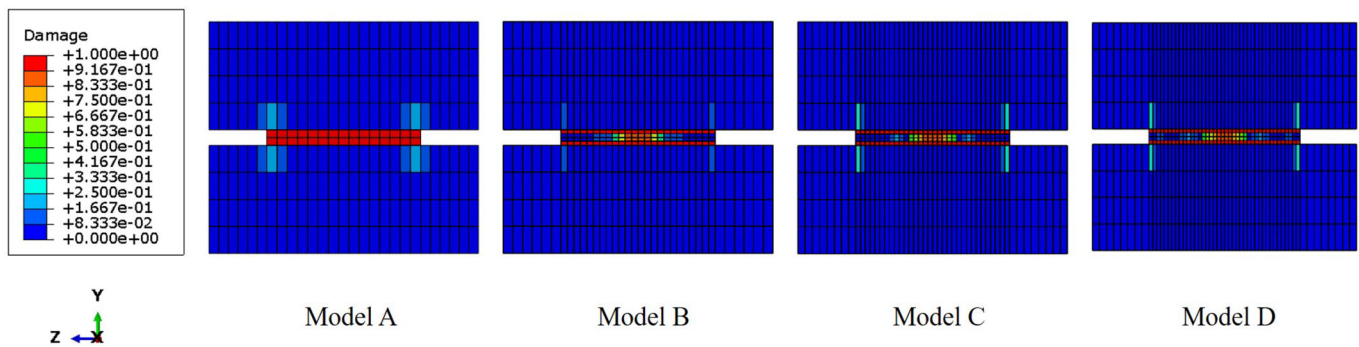
Figure 13. Final damage distribution for each model.
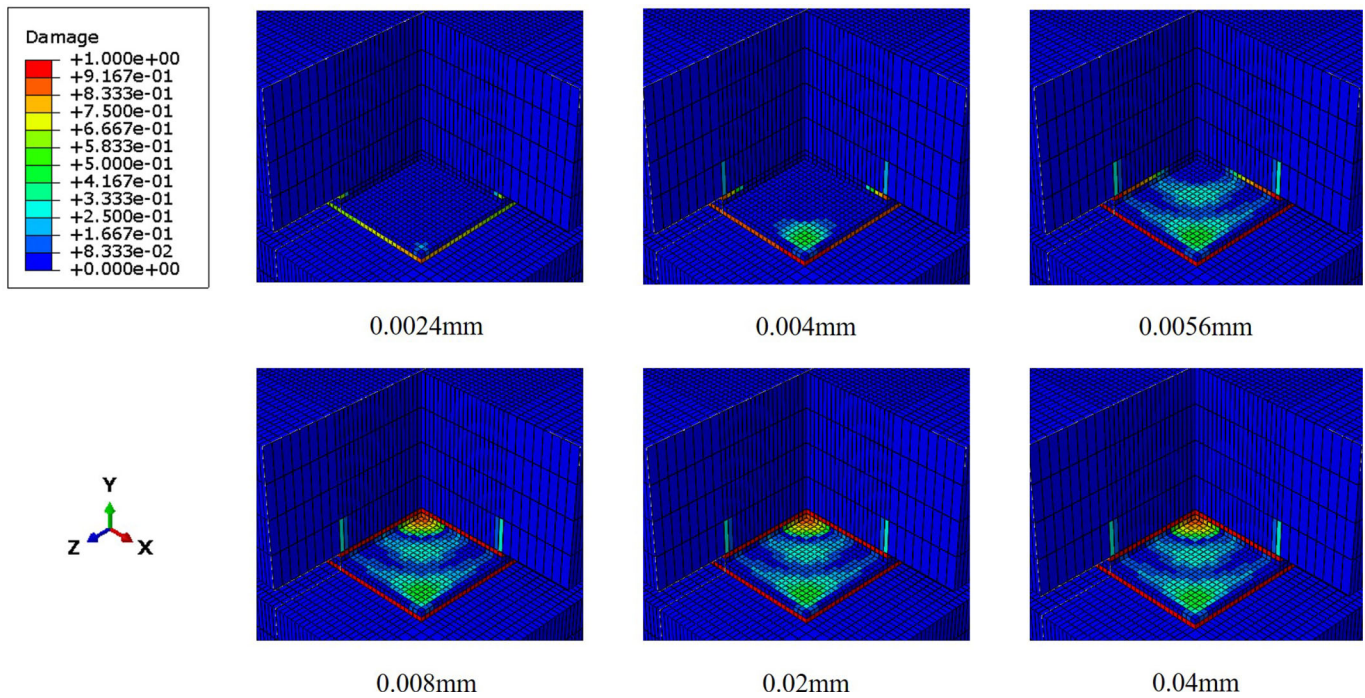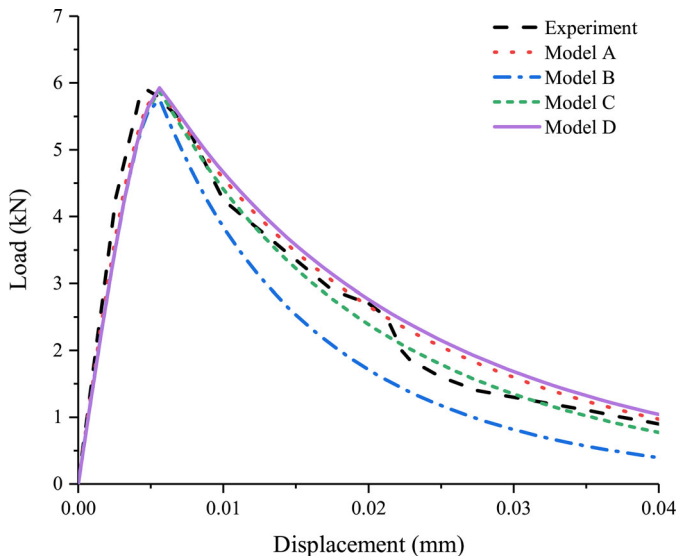
Figure 14. Damage propagation for Model D.

Figure 15. Load-displacement curves from the Hassanzadeh test.

used in the rest three models so that the corresponding L_c is smaller than the beam element size, resulting in the distributed damage can be seen in the middle. Therefore, it is more recommended to use higher-order beam elements. Otherwise, more beam elements are needed if the linear element is adopted. Moreover, except for Model A, the damage distribution is quite similar in Model B, Model C, and Model D, which shows the mesh independence.

Figure 14 displays the damage evolution from several load steps. The damage first occurs around the corner on the notched edges, and then evolutes to the middle. Then, the specimen fails due to the middle area is damaged, which corresponds to the peak load. After that, the damage stops propagation and structural behavior begins softening.

The reaction load and displacement curves from the experiment and simulations can be plotted in Figure 15. The initial stiffness from the experiment shows slightly higher than that from simulations. However, the peak loads from all simulations are close to the experimental peak load. For the softening part, three curves except for the curve from Model B are close to the experimental softening curve. That is because Model B does not fully satisfy Eq. (23). Model C adopts the same number of Lagrange elements but with higher order, which makes this mesh configuration closer to the requirement of Eq. (23). Model A and Model D meet the requirement of Eq. (23) strictly so that they are close to each other, demonstrating simulation results are independent of the mesh size using the fracture energy regularization. In other words, meeting Eq. (23) as far as possible is necessary to get a mesh independence result.

carried out here. The material properties reported in [44] are listed in Table 4. The fracture energy G_f can take 73.35 N/m from [45].

Figure 12 displays the mesh assignments on each specimen. Similarly, four kinds of configurations are taken to verify the mesh independence. In this case, the order of Lagrange elements and beam elements are not always the same and more combinations are adopted. Table 5 lists all information about meshes.

Figure 13 shows the final damage distribution obtained from four different models. In Model A, only one B2 element with a length of 4 mm is taken in the middle. The middle L_c from Model A is also 4 mm, illustrating the damage width equals 4 mm and further leading to the whole middle area being damaged. However, one higher-order beam element is

5.3. Three-point bending test

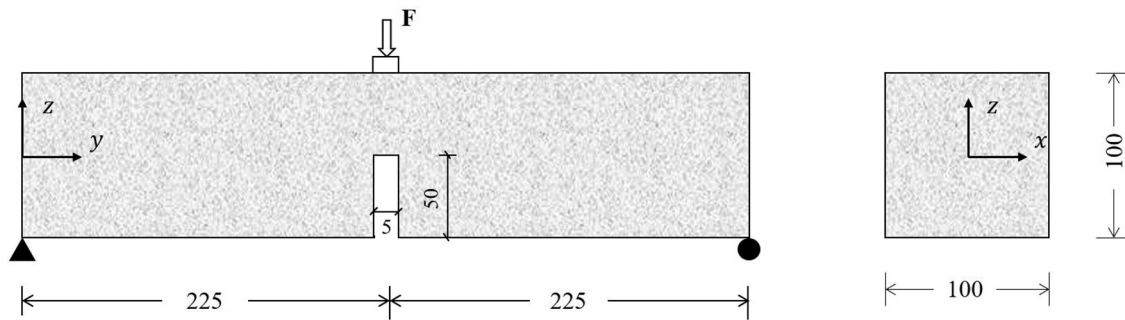Another indirect tension test is the three-point bending (TPB) test performed on notched concrete beams. One typical

Figure 16. Dimensions of the notched beam for TPB test (Unit: mm).

Table 6. Material properties of concrete in TPB test.

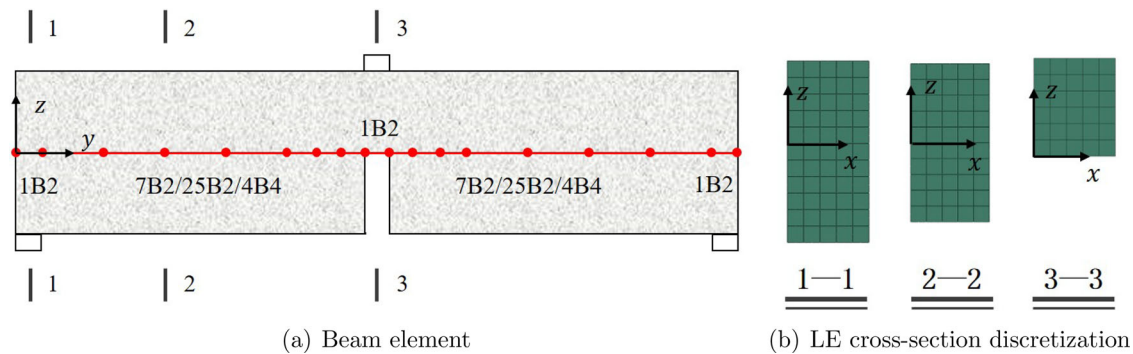| Material	E (GPa)	f_{ctm} (MPa)	f_{cm} (MPa)	υ
Concrete	20	2.4	28	0.2

(a) Beam element (b) LE cross-section discretization

Figure 17. Mesh assignment of the notched beam in TPB test.

Table 7. Beam element configuration for TPB test.

Model No.	Model 1	Model 2	Model 3
Beam element	3B2 + 14B2	3B2 + 50B2	3B2 + 8B4
L_c in the midspan (mm)	5.00	5.00	5.00
Total DOFs	12,870	37,950	19,800

notched concrete beam, shown in Figure 16, was experimentally tested in [46]. The crack thickness and depth are 5 mm and 50 mm, respectively. The material properties from experiments are listed in Table 6. The experimental fracture energy from [46] is 113 N/m. However, the simulated post-peak parts of the load-displacement curve from [47, 48] were above the experimental curve when 113 N/m was taken. Furthermore, the same notched concrete beam was studied in [49] and fracture energy in the range of $50 - 150$ N/m was recommended to consider the material scatter in properties. Inspired by [38] where the reduced fracture energy was adopted to obtain the desired load-displacement curve, the fracture energy will be taken as 75 N/m in this case.

Figure 17 shows the mesh assignment of a notched concrete beam. To reduce the computational cost, symmetry considerations are adopted. One beam element with a length of 5 mm is fixed on both two ends and in the middle notch because of their short lengths. The rest beam elements are assigned as needed. However, more beam elements should be assigned near the notch. Three kinds of beam element configurations are listed in Table 7. For cross-section, L9 elements with a side length of 10 mm are adopted for all models, which is shown in Figure 17(b), to ensure the mesh size around the notch meets the requirement of Eq. (23).

Figure 18 shows the damage propagation around the notched part. It is expected that the damage emerges from the notch tip and propagates vertically along the line of symmetry.

The reaction load and displacement curves are displayed in Figure 19 and experimental results are also plotted for comparison. From the reaction load, the numerical results are consistent with the upper and lower experimental results. Model 1 shows higher stiffness than the other two, illustrating Model 1 is not enough to meet the convergence. Increasing the number of B2 elements such as Model 2 or using higher-order beam elements such as Model 3 can solve this problem. For the softening part, numerical curves also agree with the experimental results and are between the upper and lower bound of the experimental campaign.

6. Conclusions

In this work, a modified Mazars damage model using fracture energy regularization and higher-order beam theories based on CUF are adopted to study the concrete damage
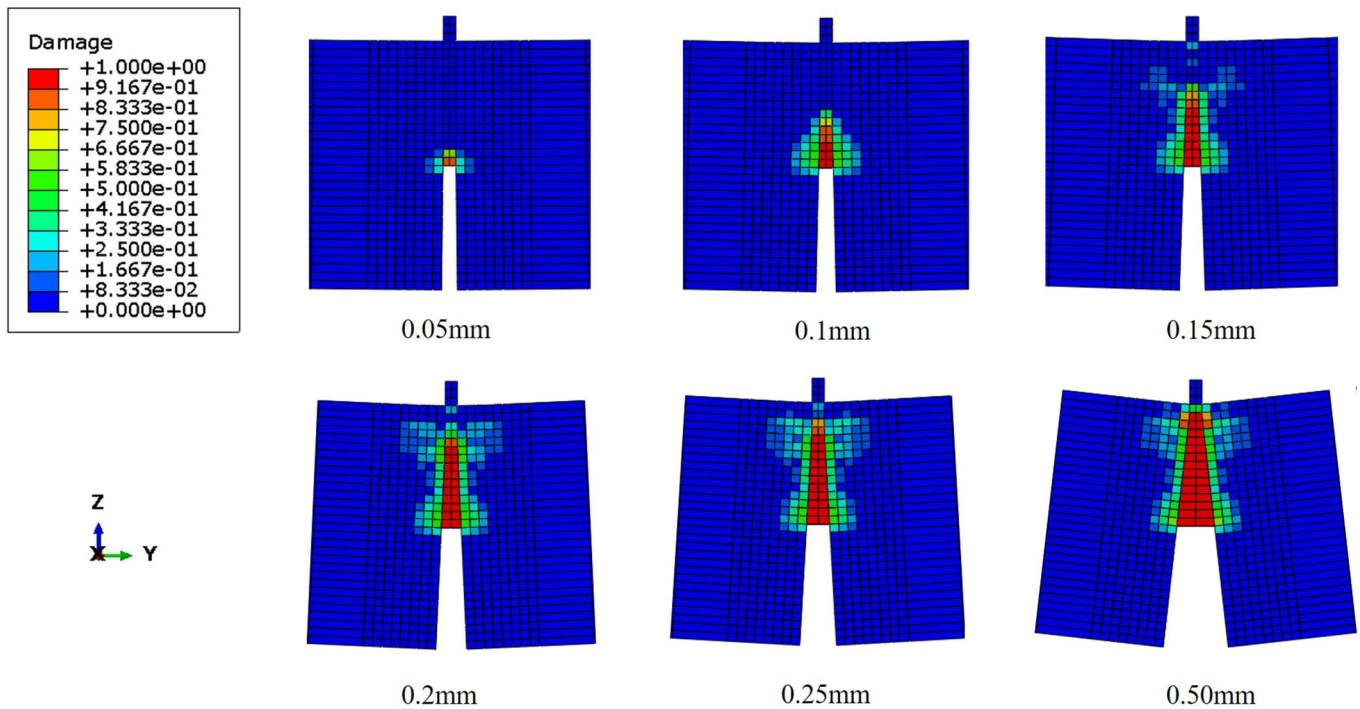
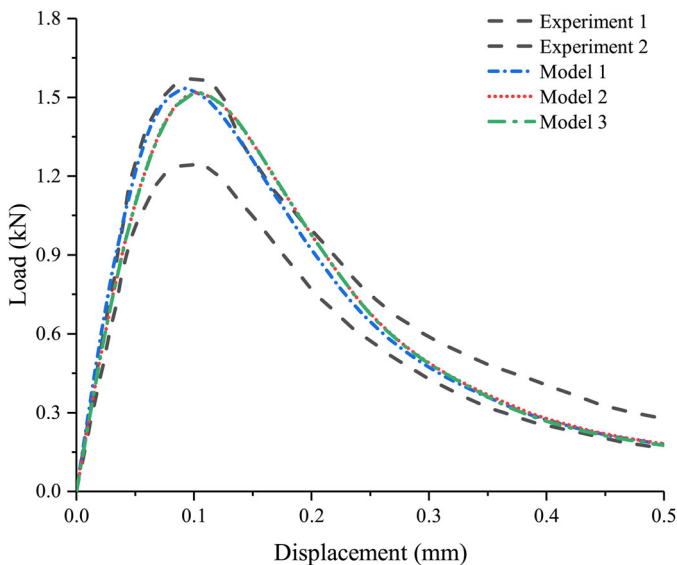Figure 18. Damage propagation near the notch for Model 3.

Figure 19. Load-displacement curves from the TPB test.

propagation. The concrete damage evolution laws are obtained from tension and compression constitutive laws from Model Code 2010. A new method for calculating characteristic element length, important for fracture energy regularization, is discussed in higher-order beam theories. By comparing the numerical results and experimental results from three well-known benchmark experiments, the following conclusions can be obtained:

1. CUF model with a random combination of LEs and beam elements provides 3D accuracy with low computational costs for concrete damage modeling.
2. The proposed CUF model with a modified Mazars damage model can simulate the structural response accurately, such as stiffness, load capacities, and softening curves, in terms of load and displacement curves.
3. The proposed CUF model can also simulate the damage propagation and crack pattern distribution in 3D, which is consistent with the experimental observations.
4. The proposed calculation of characteristic element length in the CUF model is correct and worth promoting for further application to obtain mesh independence.

Although the robust and accurate results can be obtained from the present model, the requirement from Eq. (23) is not always easy to meet, which further leads to some errors. In some particular cases, small elements are needed to meet Eq. (23) when the notch size is quite small so that the total DOFs will become considerably large. Therefore, the ongoing study will investigate the available approaches to get rid of the dependency on Eq. (23). Besides, the plain concrete structures are few in real applications. The reinforced concrete structures will also be studied soon.

Funding

ORCID

A. Pagani (iD) http://orcid.org/0000-0001-9074-2558

References

[1] A. Dragon and Z. Mroz, A continuum model for plastic-brittle behaviour of rock and concrete, Int. J. Eng. Sci., vol. 17, no. 2, pp. 121–137, 1979. DOI: 10.1016/0020-7225(79)90058-2.

[2] J. Mazars, *Application de la mécanique de l'endommagement au comportement non linéaire et à la rupture du béton de structure*, PhD thesis, Université Pierre et Marie Curie Paris 6, 1984.

[3] J. Mazars, A model of a unilateral elastic damageable material and its application to concrete. In: Fracture Toughness and Fracture Energy of Concrete, Elsevier Science Publishers, Amsterdam, The Netherlands, pp. 61–71, 1986.

[4] S. Ramtani, Y. Berthaud, and J. Mazars, Orthotropic behavior of concrete with directional aspects: Modelling and experiments, Nucl. Eng. Des., vol. 133, no. 1, pp. 97–111, 1992. DOI: 10.1016/0029-5493(92)90094-C.

[5] D. Halm and A. Dragon, A model of anisotropic damage by mesocrack growth; unilateral effect, Int. J. Damage Mech., vol. 5, no. 4, pp. 384–402, 1996. DOI: 10.1177/105678959600500403.

[6] J. Lee and G. L. Fenves, Plastic-damage model for cyclic loading of concrete structures, J. Eng. Mech., vol. 124, no. 8, pp. 892–900, 1998. DOI: 10.1061/(ASCE)0733-9399(1998)124:8(892).

[7] L. Jason, A. Huerta, G. Pijaudier-Cabot, and S. Ghavamian, An elastic plastic damage formulation for concrete: Application to elementary tests and comparison with an isotropic damage model, Comput. Methods Appl. Mech. Eng., vol. 195, no. 52, pp. 7077–7092, 2006. DOI: 10.1016/j.cma.2005.04.017.

[8] J. Y. Wu, J. Li, and R. Faria, An energy release rate-based plastic-damage model for concrete, Int. J. Solids Struct., vol. 43, no. 3–4, pp. 583–612, 2006. DOI: 10.1016/j.ijsolstr.2005.05.038.

[9] S. T. Pietruszczak and Z. Mroz, Finite element analysis of deformation of strain-softening materials, Int. J. Numer. Methods Eng., vol. 17, no. 3, pp. 327–334, 1981. DOI: 10.1002/nme.1620170303.

[10] Z. Bažant, Nonlocal damage theory based on micromechanics of crack interactions, J. Eng. Mech., vol. 120, no. 3, pp. 593–617, 1994. DOI: 10.1061/(ASCE)0733-9399(1994)120:3(593).

[11] G. Borino, B. Failla, and F. Parrinello, A symmetric nonlocal damage theory, Int. J. Solids Struct., vol. 40, no. 13–14, pp. 3621–3645, 2003. DOI: 10.1016/S0020-7683(03)00144-6.

[12] R. H. J. Peerlings, M. G. D. Geers, R. De Borst, and W. A. M. Brekelmans, A critical comparison of nonlocal and gradient-enhanced softening continua, Int. J. Solids Struct., vol. 38, no. 44–45, pp. 7723–7746, 2001. DOI: 10.1016/S0020-7683(01)00087-7.

[13] Z. P. Bažant and J. L. Le, Probabilistic Mechanics of Quasibrittle Structures: Strength, Lifetime, and Size Effect, Cambridge University Press, Cambridge, England, 2017.

[14] G. Pijaudier-Cabot and F. Dufour, Non local damage model: Boundary and evolving boundary effects, Eur. J. Environ. Civil Eng., vol. 14, no. 6–7, pp. 729–749, 2010. DOI: 10.1080/19648189.2010.9693260.

[15] A. Hillerborg, M. Modéer, and P. E. Petersson, Analysis of crack formation and crack growth in concrete by means of fracture mechanics and finite elements, Cem. Concr. Res., vol. 6, no. 6, pp. 773–781, 1976. DOI: 10.1016/0008-8846(76)90007-7.

[16] Z. P. Bažant and B. H. Oh, Crack band theory for fracture of concrete, Mat. Constr., vol. 16, no. 3, pp. 155–177, 1983. DOI: 10.1007/BF02486267.

[17] J. L. Le and J. Eliáš, A probabilistic crack band model for quasibrittle fracture, Trans. ASME, J. Appl. Mech., vol. 83, no. 5, p. 051005, 2016. DOI: 10.1115/1.4032692.

[18] A. Gorgogianni, J. Eliáš, and J. L. Le, Mechanism-based energy regularization in computational modeling of quasibrittle fracture, Trans. ASME, J. Appl. Mech., vol. 87, no. 9, p. 091003, 2020. DOI: 10.1115/1.4047207.

[19] G. Pijaudier-Cabot and J. Mazars, Damage models for concrete, Handbook of Materials Behavior Models, vol. 2, pp. 500–512, 2001. DOI: 10.1016/B978-012443341-0/50056-9.

[20] J. Mazars, F. Hamon, and S. Grange, A new 3d damage model for concrete under monotonic, cyclic and dynamic loadings, Mater. Struct., vol. 48, no. 11, pp. 3779–3793, 2015. DOI: 10.1617/s11527-014-0439-8.

[21] M. R. T. Arruda, J. Pacheco, L.M. S. Castro, and E. Julio, A modified mazars damage model with energy regularization, Eng. Fract. Mech., vol. 259, p. 108129, 2022. DOI: 10.1016/j.engfracmech.2021.108129.

[22] L. Taerwe and S. Matthys, fib Model Code for Concrete Structures 2010, John Wiley & Sons, Ltd, Hoboken, New Jersey, 2013. DOI: 10.1002/9783433604090.ch5

[23] E. Carrera, G. Giunta, and M. Petrolo, Beam Structures: Classical and Advanced Theories, John Wiley & Sons, Hoboken, New Jersey, 2011.

[24] W. A. Oldfather, C. A. Ellis, and D. M. Brown, Leonhard Euler's elastic curves, Isis, vol. 20, no. 1, pp. 72–160, 1933. DOI: 10.1086/346767.

[25] S. P. Timoshenko, Lxvi. On the correction for shear of the differential equation for transverse vibrations of prismatic bars, Lond. Edinb. Dublin Philos. Mag. J. Sci., vol. 41, no. 245, pp. 744–746, 1921. DOI: 10.1080/14786442108636264.

[26] E. Carrera, M. Cinefra, M. Petrolo, and E. Zappino, Finite Element Analysis of Structures through Unified Formulation, Wiley Online Library, Hoboken, New Jersey, 2014.

[27] R. Azzara, E. Carrera, and A. Pagani, Nonlinear and linearized vibration analysis of plates and shells subjected to compressive loading, Int. J. Non Linear Mech., vol. 141, p. 103936, 2022. DOI: 10.1016/j.ijnonlinmec.2022.103936.

[28] A. Pagani, M. Enea, and E. Carrera, Quasi-static fracture analysis by coupled three-dimensional peridynamics and high order one-dimensional finite elements based on local elasticity, Numer. Methods Eng., vol. 123, no. 4, pp. 1098–1113, 2022. DOI: 10.1002/nme.6890.

[29] I. Kaleel, M. Petrolo, A. M. Waas, and E. Carrera, Micromechanical progressive failure analysis of fiber-reinforced composite using refined beam models, Trans. ASME, J. Appl. Mech., vol. 85, no. 2, p. 021004, 2018. DOI: 10.1115/1.4038610.

[30] M. H. Nagaraj, J. Reiner, R. Vaziri, E. Carrera, and M. Petrolo, Progressive damage analysis of composite structures using higher-order layer-wise elements, Compos. B: Eng., vol. 190, p. 107921, 2020. DOI: 10.1016/j.compositesb.2020.107921.

[31] M. H. Nagaraj, J. Reiner, R. Vaziri, E. Carrera, and M. Petrolo, Compressive damage modeling of fiber-reinforced composite laminates using 2d higher-order layer-wise models, Compos. B: Eng., vol. 215, p. 108753, 2021. DOI: 10.1016/j.compositesb.2021.108753.

[32] E. Carrera, R. Augello, A. Pagani, and X. Xu, Component-wise approach to reinforced concrete structures, Mech. Adv. Mater. Struct., pp. 1–19, 2021. DOI: 10.1080/15376494.2021.1912442.

[33] M. R. T. Arruda, L. M. S. Castro, A. J. M. Ferreira, D. Martins, and J. R. Correia, Physically non-linear analysis of beam models using Carrera Unified Formulation, Compos. Struct., vol. 195, pp. 60–73, 2018. DOI: 10.1016/j.compstruct.2018.03.107.

[34] J. Shen, A. Pagani, M. R. T. Arruda, and E. Carrera, Exact component-wise solutions for 3d free vibration and stress analysis of hybrid steel–concrete composite beams, Thin-Walled Struct., vol. 174, p. 109094, 2022. DOI: 10.1016/j.tws.2022.109094.

[35] M. R. T. Arruda and L. M. S. Castro, Non-linear dynamic analysis of reinforced concrete structures with hybrid mixed stress finite elements, Adv. Eng. Softw., vol. 153, p. 102965, 2021. DOI: 10.1016/j.advengsoft.2020.102965.

[36] F. A. Leone and B. P. Justusson, Effects of characteristic element length on fracture energy dissipation in continuum damage mechanics models, J. Compos. Mater., vol. 55, no. 24, pp. 3551–3566, 2021. DOI: 10.1177/00219983211023790.

[37] ABAQUS, Abaqus user subroutines reference guide, 2013.

[38] M. Jirásek and M. Bauer, Numerical aspects of the crack band approach, Comput. Struct., vol. 110-111, pp. 60–78, 2012. DOI: 10.1016/j.compstruc.2012.06.006.

[39] Fédération Internationale du Béton, Practitioners Guide to Finite Element Modelling of Reinforced Concrete Structures,

State-of-Art Report, International Federation for Structural Concrete (fib), Lausanne, Switzerland, 2008.

[40] En 1992-1-1, Eurocode 2: Design of Concrete Structures, General Rules and Rules for Buildings, Vol. 3, CEN, Brussels, 2004.

[41] P. B. Shing and T. A. Tanabe, Modeling of Inelastic Behavior of RC Structures under Seismic Loads, ASCE Publications, Reston, Virginia, United States, 2001.

[42] H. Nakamura, T. Nanri, T. Miura, and S. Roy, Experimental investigation of compressive strength and compressive fracture energy of longitudinally cracked concrete, Cem. Concr. Compos., vol. 93, pp. 1–18, 2018. DOI: 10.1016/j.cemconcomp.2018.06.015.

[43] B. Winkler, Traglastuntersuchungen Von Unbewehrten Und Bewehrten Betonstrukturen Auf Der Grundlage Eines Objektiven Werkstoffgesetzes Für Beton, Innsbruck University Press, Austria, 2001.

[44] M. Hassanzadeh, Behaviour of Fracture Process Zones in Concrete Influenced by Simultaneously Applied Normal and Shear Displacements. Division of Building Materials, Lund Institute of Technology, Sweden, 1992.

[45] L. A. M. Mendes, Refined three-dimensional seismic analysis of reinforced concrete structures, PhD thesis, Instituto Superior Técnico, Universidade Técnica de Lisboa, 2011.

[46] H. W. Koermeling and H. A. Reinhardt, Determination of the fracture energy of normal concrete and epoxy modified concrete, Technical report, Stevin Lab, Delft University of Technology, 1983.

[47] J. Bobiński and J. Tejchman, Modelling of concrete behaviour with a non-local continuum damage approach, Arch. Hydro-Eng. Environ. Mech., vol. 52, no. 3, pp. 243–263, 2005.

[48] M. V. K. V. Prasad and C. S. Krishnamoorthy, Computational model for discrete crack growth in plain and reinforced concrete, Comput. Methods Appl. Mech. Eng., vol. 191, no. 25–26, pp. 2699–2725, 2002. DOI: 10.1016/S0045-7825(02)00210-4.

[49] J. G. Rots, Computational modeling of concrete fracture, PhD thesis, Delft University of Technology, 1988.